

## Yb/InSe/Sb<sub>2</sub>Te<sub>3</sub>/Au BROKEN GAP HETEROJUNCTION DEVICES DESIGNED AS CURRENT RECTIFIERS, TUNABLE MOS CAPACITORS AND GIGAHERTZ MICROWAVE CAVITIES

L. H. K. ALFHAID<sup>a</sup>, A. F. QASRAWI<sup>b,c,\*</sup>, S. E. ALGARNI<sup>d</sup>

<sup>a</sup>*Department of Physics, Collage of Science, University of Ha'il, Ha'il, Saudi Arabia*

<sup>b</sup>*Department of Physics, Arab American University, Jenin, Palestine*

<sup>c</sup>*Department of Electrical and Electronics Engineering, Istinye University, 34010, Istanbul, Turkey*

<sup>d</sup>*Department of Physics, Faculty of Science, University of Jeddah, Jeddah, Saudi Arabia*

Herein, we report the design and experimental characterization of a broken gap heterojunction devices fabricated by vacuum evaporation of Yb/InSe/Sb<sub>2</sub>Te<sub>3</sub>/Au stacked layers. The structural characterizations of the stacked layers revealed an amorphous/polycrystalline heterojunction type. The measurements of capacitance-voltage characteristics in the frequency domain of 1.0-9.0 MHz displayed tunable metal-oxide-semiconductor (MOS) characteristics. The frequency dependent built-in voltage, depletion width, and free carrier density is also investigated. In addition, the analyses of current-voltage characteristics have shown that the device displays highly stable current rectification ratios of  $\sim 10^3$  above 0.20 V. Moreover, the ac signal analyses in the frequency domain of 10-1800 MHz have shown the possible tunability of the conductance and capacitance over a wide range of frequency. Furthermore, the microwave cutoff frequency spectra indicated increasing cutoff frequency limits with increasing incident signal frequency. The microwave cutoff frequency reached 7.1 GHz for a propagating signal of frequency of 1800 MHz.

(Received January 31, 2021; Accepted March 5, 2021)

*Keywords:* InSe/Sb<sub>2</sub>Te<sub>3</sub>, Broken gap, Microwave cavity, MOS capacitors, Bandstop filter

### 1. Introduction

Antimony telluride is a smart material employable in the design of multifunctional optoelectronic devices. They exhibit novel thermoelectric properties [1]. Temperature dependent measurements of thermoelectric power on these films have shown that the antimony telluride films can reveal a thermoelectric power factor up to 1.0 mW/mK<sup>2</sup>. Antimony telluride thin films are also reported to exhibit nonlinear optical properties that nominate it for use in modes locking and super resolved direct lasers writing [3]. Germanium implanted antimony telluride thin films are also mentioned exhibiting high speed phase change memory characteristics [4]. As memory devices, a reversible switching between Set and Reset is achieved within electric pulse durations of 10 ns. In addition, Sb<sub>2</sub>Te<sub>3</sub> thin films, which were deposited by the RF sputtering technique, were reported exhibiting photovoltaic characteristics [5]. Their performance as solar cells revealed solar cell efficiency up to 8.01%.

Owing to the wide range of applications of antimony telluride, in the current study, we are motivated to focus on the design and fabrication of multifunction *pn* junction device that can carry out more than a duty at a time. For this purpose, Yb/InSe interfaces are selected as *n*-type substrates to be coated with *p*-type Sb<sub>2</sub>Te<sub>3</sub> films. The Yb/InSe is selected as substrate because of its smart properties as dielectric resonators [6]. In our earlier studies we have shown that the interfacing between Yb and InSe results in enhancing the light absorbability [6]. This type of interfacing enhanced the drift mobility of electrons in the lateral direction of the films and formed a band offset of  $\sim 0.27$  eV. When the Yb/InSe substrates were contacted with carbon, Schottky diodes were formed. The diodes displayed current rectification ratios ("on/off") of 18.8 [6]. For

\* Corresponding author: atef.qasrawi@aaup.edu  
<https://doi.org/10.15251/CL.2021.183.113>

these reasons, we attempted to fabricate a *pn* structure that reveals higher current rectification ratios and that can handle other issues when operated in passive modes. Particularly, the constructed Yb/*n*-InSe/*p*-Sb<sub>2</sub>Te<sub>3</sub>/Au will be characterized by means of X-ray diffraction, current-voltage characteristics and frequency dependent capacitance-voltage characteristics. In addition, the capacitance, conductance and microwave cutoff frequency spectra in the frequency domain of 10-1800 MHz will be considered and the possible applications of the device will be suggested.

## 2. Experimental details

InSe thin films of thicknesses of 500 nm are grown from high purity (99.99%)  $\alpha$ -In<sub>2</sub>Se<sub>3</sub> crystal lumps in a NORM VCM-600 vacuum evaporator under pressure of 10<sup>-5</sup> mbar. The films are coated onto Yb substrates. The Yb substrates were prepared by the same method onto an ultrasonically and chemically cleaned glass slides. The fabricated Yb/InSe films were masked and coated with high purity Sb<sub>2</sub>Te<sub>3</sub> thin films. The thickness of Sb<sub>2</sub>Te<sub>3</sub> thin films was 300 nm. The resulting Yb/InSe/Sb<sub>2</sub>Te<sub>3</sub> films were coated with gold pads of areas of 3.14 × 10<sup>-2</sup> cm<sup>2</sup>. The schematics of the device with Au pads are illustrated in the inset of Fig. 1. Inficon STM-2 thickness monitors was used to measure the films thicknesses. The thickness was confirmed with surface roughness tester-profilometer (Model SOLID TR-200 plus). The electrical characterizations were handled with the help of Keithley current-voltage characteristics system. The system is composed of Keithley 230 voltage source and Keithley 6485 Picoammeter. The impedance spectroscopy measurements were carried out using Agilent 4291B 0.01-1.80 GHz impedance analyzer.

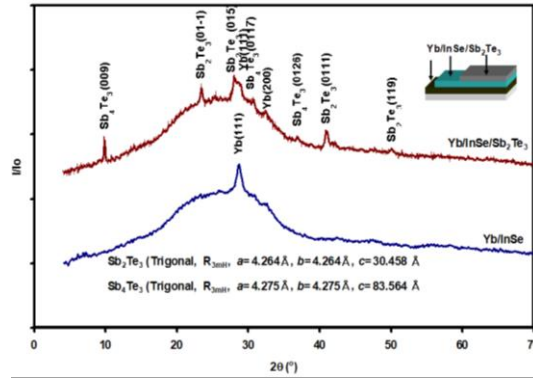


Fig. 1. The X-ray diffraction patterns for Yb/InSe and Yb/InSe/Sb<sub>2</sub>Te<sub>3</sub> heterojunctions. The inset shows the schematics of the heterojunctions.

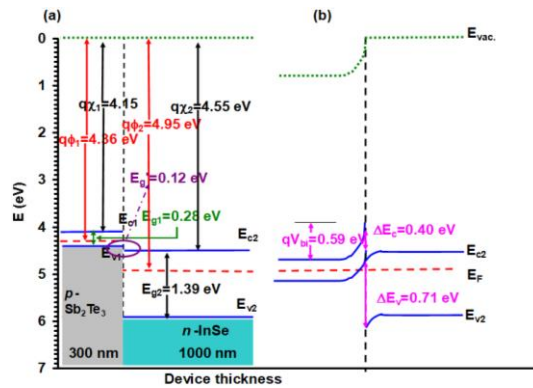


Fig. 2. The energy band diagram at thermal equilibrium (a) before and (b) after the junction of InSe and Sb<sub>2</sub>Te<sub>3</sub> interfaces.

### 3. Results and discussion

The schematics of the Yb/InSe/Sb<sub>2</sub>Te<sub>3</sub>/Au devices are shown in the inset of Fig. 1. The figure also displays the X-ray diffraction (XRD) patterns for the Yb/InSe substrates and for the Yb/InSe/Sb<sub>2</sub>Te<sub>3</sub> heterojunctions. The XRD patterns of Yb/InSe display only one intensive peak. This peak which is centered at diffraction angles of  $2\theta = 28.55^\circ$  is assigned to cubic closed packed ytterbium. The main reflection planes of cubic Yb are oriented in the (111) direction revealing a lattice constant of  $a = 5.411 \text{ \AA}$ . The value of the lattice constant is consistent with the PDF card number 00-002-1367. The absence of sharp diffraction peaks of InSe indicates the amorphous nature of the InSe layers. On the other hand, as seen from Fig. 1, coating of Sb<sub>2</sub>Te<sub>3</sub> layers onto the surface of InSe resulted in the appearance of many other diffraction peaks. These sharp patterns were analyzed with the help of ‘‘Crystdiff’’ software packages and compared to the existing PDF cards of Te (JCPDS Card No. 36-1452), Sb (JCPDS card no. 85-1324), Sb<sub>2</sub>Te<sub>3</sub> (JCPDS card No. 15-0874), Sb<sub>4</sub>Te<sub>3</sub> and InSe (card No.: 34-1431). Investigations of the crystal structures of these materials indicated that all the sharp reflection peaks are assigned to hexagonal ( $a = b = 4.264 \text{ \AA}$ ,  $c = 30.485 \text{ \AA}$ ,  $\gamma = 120^\circ$ ) Sb<sub>2</sub>Te<sub>3</sub> [7] and hexagonal ( $a = b = 4.275 \text{ \AA}$ ,  $c = 83.564 \text{ \AA}$ ,  $\gamma = 120^\circ$ ) Sb<sub>4</sub>Te<sub>3</sub> (crystallography open database COD: 7113353). Thus, the resulting interfaced structure is composed of amorphous/polycrystalline interfaces. These structures are known to exhibit good optoelectronic properties [8] in which when used in the fabrication of solar cells they reveal high open circuit voltage values [9].

The formation of Sb<sub>4</sub>Te<sub>3</sub> phases on surface of Yb/InSe is ascribed to the bonding mechanism. Similar to the bonding properties of (Bi<sub>2</sub>Se<sub>3</sub>)<sub>m</sub>(Bi<sub>2</sub>) The layered Sb<sub>2</sub>Te<sub>3</sub> crystals are mentioned being composed of quintuple layers stacked along the (0001) direction of the hexagonal unit cell. Each of the quintuple layers is created by five covalently bonded Te-Sb-Te-Sb-Te atomic sheets. Strong interactions between the atomic sheets exist within a quintuple layer. However, the interactions between two adjacent quintuple layers are dominated by the weak van der Waals forces. Hence, the cleaving planes are centered between the quintuple layers and terminated with Te atomic layers on the surface. In Sb<sub>4</sub>Te<sub>3</sub>, two extra Sb layers are added to the sequence of stacking order owing to richness of Sb that results from breaking the weaker bonds in a neighboring quintuple layers [10].

From energy bands point of view, Sb<sub>2</sub>Te<sub>3</sub> exhibits an electron affinity ( $q\chi_1$ ) of 4.15 eV, energy band gap ( $E_{g1}$ ) of 0.28 eV [11] and work function ( $q\phi_1$ ) of  $\sim 4.36$  eV (assuming a Fermi level ( $E_F$ ) at 0.07 eV above the valence band ( $E_v$ )). The respective values of electron affinities ( $q\chi_2$ ), energy band gap ( $E_{g2}$ ) and work function ( $q\phi_2$ ) of InSe are 4.55 eV, 1.39 eV and 4.95 eV [6]. The conduction and valence bands offsets are  $\Delta E_c = |q\chi_2 - q\chi_1| = 0.40$  eV and  $\Delta E_v = |E_{g2} - E_{g1} - \Delta E_c| = 0.71$  eV, respectively. The band structure of the device is illustrated in Fig. 2 (a). As can be seen from the energy band diagram, the valence band edge of Sb<sub>2</sub>Te<sub>3</sub> is at 4.43 eV. It is above the edge of the conduction band of InSe (4.55 eV). The numerical data suggests that the formed Yb/InSe/Sb<sub>2</sub>Te<sub>3</sub> heterojunctions are of broken gap type. The separation between valence bands edges of Sb<sub>2</sub>Te<sub>3</sub> and conduction band edge of InSe forms a new gap of  $E'_g = 0.12$  eV. This type of heterojunction devices are special type of staggered heterojunctions. In staggered type heterojunctions the positions of the lower  $E_c$  and higher  $E_v$  are dislocated so that electrons are collected at lower  $E_c$  and holes are collected at higher valence band edges [12]. In the broken gap heterojunctions  $E_c$  of InSe is lower than  $E_v$  of Sb<sub>2</sub>Te<sub>3</sub> forcing an overlap between the conduction band of InSe with valence band of Sb<sub>2</sub>Te<sub>3</sub>. Such type of heterojunction devices were nominated as promising devices for spintronic and nanoelectronic applications [13]. The band bending, vacuum level lowering and thermal equilibrium of Fermi levels are shown in Fig. 2 (b). The figure additionally illustrates the built in potential of the device ( $qV_{bi} = |q\phi_2 - q\phi_1|$ ) which exhibit value of 0.59 eV under no voltage biasing conditions. This parameter is the main factor that control the operation mode of the device [12].

From practical point of view, as a passive mode device, the Yb/InSe/Sb<sub>2</sub>Te<sub>3</sub>/Au heterojunctions are imposed between the terminals of an impedance analyzer and subjected to dc biasing in the frequency domain of 1.0-9.0 MHz. The measured capacitance ( $C$ )–voltage ( $V$ )

characteristics is shown in Fig. 3 (a). As seen from the figure, the capacitance value is low and constant under reverse voltage ( $V_R$ ) biasing in the ranges of  $-2.0 < V_R \leq 0$  V. The capacitance values increases with increasing forward voltage ( $V_F$ ) in the voltage range of  $0.0 < V_F < 0.60$  V. For higher forward voltages, the capacitance value are high and remain constant regardless of the voltage value. Operational modes in which  $C$  remains low and constant under  $V_R$  are related to accumulation modes. Those in which  $C$  increases with increasing  $V_F$  are related to the depletion mode. When the  $C - V$  characteristics displays high and frequency invariant  $C$  values, the device is said to have reached the weak inversion mode. When  $V_F = 2V_{bi}$  the device reaches the strong inversion mode. The operation mode of the device which appears in Fig. 3(a) indicate that it exhibit metal-oxide-semiconductor (MOS) characteristics [12, 14].

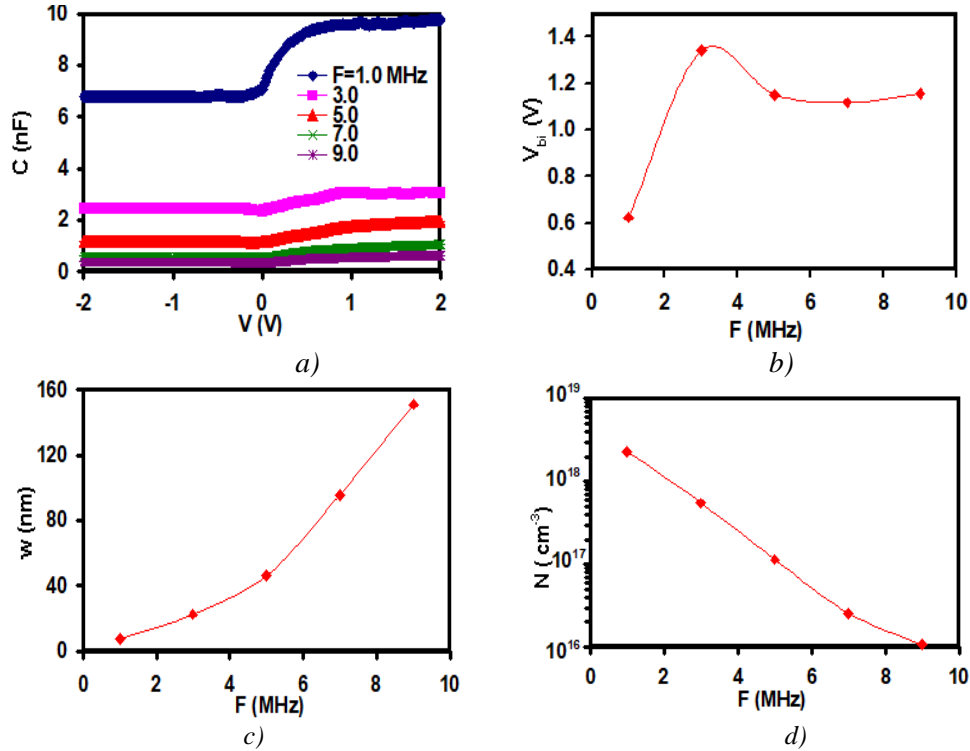


Fig. 3. (a) the capacitance ( $C$ )-voltage ( $V$ ) characteristic curves, (b) the built-in voltage, (c) the free carrier density and (d) the depletion width variations as function of signal frequency for the Yb/InSe/Sb<sub>2</sub>Te<sub>3</sub>/Au MOS devices.

As also seen from Fig. 3 (a), for the Yb/InSe/Sb<sub>2</sub>Te<sub>3</sub>/Au MOS devices, increasing the frequency decreases the capacitance level. As for examples, at  $V_R = -1.0$  V and  $F = 1.0$  MHz, the capacitance exhibit value of 6.8 nF. This value decreases to 2.3 nF when the  $C - V$  characteristics is recorded at frequency value of 3.0 MHz and reaches value of 0.38 nF at 9.0 MHz. Since in the range of applied voltage the capacitance refers to the geometrical value, the inability of the device to polarize with the signal frequency could account for the decrease in  $C$  values with increasing  $F$ . On the other hand, analysis of the  $C - V$  characteristics in the depletion region in accordance with the equation [12],

$$C^{-2} = \frac{2(V_{bi} - V - \frac{kT}{q})}{(qA^2\epsilon_{pn}N)} \quad (1)$$

Allow determining the built in voltage under voltage biasing. In the equation,  $A=0.0314$  cm<sup>2</sup> is the device area,  $N$  is the free carrier density,  $kT/q$  is the thermal energy and  $\epsilon_{pn}$  is the dielectric constant of the  $pn$  junction.  $\epsilon_{pn}^{-1} = (\epsilon_{Sb_2Te_3}^{-1} + \epsilon_{Yb/InSe}^{-1})^{-1} = 1.90$ . The high frequency

dielectric constants of  $\text{Sb}_2\text{Te}_3$  and  $\text{Yb/InSe}$  are taken to be 3.7 [15] and 3.9 [6], respectively. Plotting  $C^{-2} - V$  variations in the studied frequency domain and in the range of  $0.0 < V_F < 0.60$  V, allow determining the built-in voltage, free carrier density and depletion width ( $w = \sqrt{2 \epsilon_{pn} (V_{bi} - V)/(qN_a)}$ ) as well. The frequency dependencies of the  $V_{bi}$ ,  $N_a$  and  $w$  are shown in Fig. 3 (b), (c) and (d), respectively. It is clear from the  $V_{bi} - F$  variations that the built in voltage exhibits value of 0.62 V and increases with increasing signal frequency reaching a value of  $\sim 1.15$  V at 5.0 MHz. It then remains constant regardless of the frequency value. The low frequency built-in voltage values being 0.62 V is very close to the theoretically estimated though the design of the energy bands diagrams. On the other hand, as appears in Fig. 3 (c), the free carrier density exponentially decreases with increasing signal frequency. Changing the signal frequency from 1.0 to 9.0 MHz decreased the free charge carrier density by three orders of magnitude. It is also noticeable from Fig. 3 (d), that the depletion width of the device increases with increasing signal frequency. The depletion width increases from 7.5 nm to 151 nm as the frequency increases from 1.0 to 9.0 MHz. The response of  $N$  and  $w$  to the variation in the signal frequency is consistent. It was reported that the deeper the donors levels, the harder the ionization of them, and the wider the depletion layer will be [16]. When  $w$  is very wide, the charge carriers cannot move through it to align the relevant energy levels at the edges of the dipole layer. This could be one main reason for the unvaried built-in voltage when frequency increases [16]. The  $\text{Yb/InSe/Sb}_2\text{Te}_3/\text{Au}$  MOS device parameters which are shown in Fig. 3 (a)-(d) indicate the possible tunability of the device by fixing the signal frequency [12].

Fig. 4 (a) illustrates the current ( $I$ )-voltage ( $V$ ) characteristics for the  $\text{Yb/InSe/Sb}_2\text{Te}_3/\text{Au}$  devices. The forward current was supplied from the  $\text{Sb}_2\text{Te}_3$  side. Large difference between the forward and reverse biased currents can be observed.

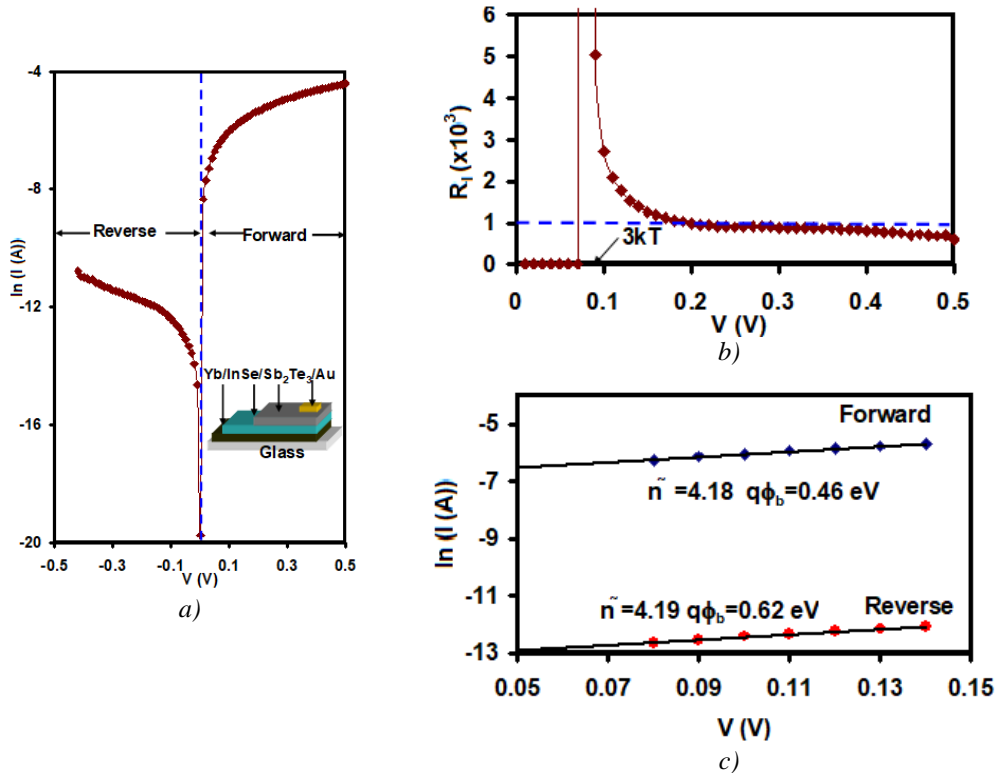


Fig. 4. (a) the current ( $I$ )-voltage ( $V$ ) characteristics, (b) the current rectification ratio and (c) the  $\ln(I) - V$  variations for  $\text{Yb/InSe/Sb}_2\text{Te}_3/\text{Au}$  broken gap heterojunction devices.

The “on/off” (forward/reverse) ratios which is known as current rectification ratios ( $R_I = I_{\text{Forward}}/I_{\text{Reverse}}$ ) as function of biasing voltage is illustrated in Fig. 4 (b). As seen from

the figure, at biasing voltages near  $\frac{3kT}{q} \approx 0.08 V$ ,  $R_I$  is very high and exceeds  $6 \times 10^3$ . The value  $qV = 3kT$  relates to the minimum energy needed to pick up electrons from the top of the valance band. For all applied voltages larger than  $\frac{3kT}{q}$  electrons can move in the devices by thermionic emission over the energy barriers [12, 17]. The current rectification ratio sharply decreases with increasing applied voltage in the range of  $0.08 < V < 0.19 V$ . It then remains constant exhibiting a value of  $\sim 10^3$  over a wide range of voltage. This property of the device means the ability of using it as electronic switches in a wide range of voltage. Investigations on the current conduction mechanisms by the thermionic emission theory allowed determining the energy barrier height ( $q\phi_b$ ) and ideality factor ( $\tilde{n}$ ) of the  $pn$  junction. For this purpose Richardson -Schottky equation,

$$I = AA^*T^2 \exp\left(-\frac{q\phi_b}{kT}\right) \left(\exp\left(-\frac{qV}{\tilde{n}kT}\right) - 1\right), \quad (2)$$

was employed. In Eqn. (2),  $A^* = 120m_{pn}^*$  is Richardson constant. The effective mass  $m_{pn}^*$  is calculated from the relation,  $m_{pn}^* = ((m_{Sb_2Te_3}^*)^{-1} + (m_{InSe}^*)^{-1})^{-1}$ , through inserting the value of the effective mass of electrons as  $0.156m_o$  [6] for InSe and the value of effective mass of holes as  $0.590m_o$  [18]. The value of  $m_{pn}^*$  is found to be  $0.123m_o$ . The linear plots which are shown in Fig. 4 (c), allowed determining the values of  $\tilde{n}$  and  $q\phi_b$  as 4.18 and 0.46 eV under forward biasing conditions and as 4.19 and 0.62 eV under reverse biasing conditions, respectively.

It is interesting to observe that the barrier height value under reverse biasing conditions is, approximately, equal to the built-in potential value which was determined from the  $C - V$  analyses ( $F=1.0$  MHz) and equal to the theoretically estimated one (illustrated in Fig. 2 (b)). In general, the barrier height is related to the built in potential through the relation [12, 17],

$$q\phi_b = qV_{bi} + kT + qV_n \quad (3)$$

Here,  $qV_n = kT \ln(N_c/N)$  is selected because of the broken gap property of the heterojunction which indicate that all energy bands (valence and conduction) are located above the conduction band of InSe (Fig. 2 (a)). In the equation,  $N_c = 4.81 \times 10^{15} (m_{InSe}^* T)^{\frac{3}{2}} = 1.54 \times 10^{18} cm^{-3}$  is the density of states in the conduction band and  $N = N_d - N_a = 2.31 \times 10^{18} cm^{-3}$  at (1.0 MHz as an example) is the difference between the donors ( $N_d$ ) and acceptors ( $N_a$ ) densities of states below and above the conduction and valence bands, respectively.  $N - F$  variations are shown in Fig. 3 (c). The calculated  $qV_n$  value at 1.0 MHz is -0.011 eV. It reaches value of 0.139 eV at 9.0 MHz. The barrier height is equal to the built in potential owing to the high free carrier density at low frequency values. At high frequencies the barrier height which is determined from the capacitance- voltage characteristics could reach 1.32 eV. Thus, large tuning of barrier height is also possible via frequency change.

The deviation of the ideality factor  $\tilde{n}$  from unity can be ascribed to the generation – recombination mechanisms of charge carriers in the depletion layer, parasitic voltage drop due to high series resistance and the tunneling of charge carriers through the subgap  $E'_g$  (Fig. 2 (a)) [12, 17]. In addition, existence of the interfacial layers in the films, barrier inhomogeneous or wide distribution of low-barrier height patches leads to the formation of interface states and thus accounts for the deviation of ideality factor from unity [11].

Fig. 5 (a), (b) and (c) illustrates the conductance ( $G$ ), capacitance and microwave cutoff frequency ( $f_{co} = G/(2\pi C)$ ) spectra for the Yb/InSe/Sb<sub>2</sub>Te<sub>3</sub>/Au devices. The three parameters are recorded in the frequency domain of 10-1800 MHz. It is clear from Fig. 5 (a) that the conductance increase with increasing signal frequency in the frequency domain of 10-300 MHz, it then decreases with increasing frequency value in the range of 300-500 MHz. In the range of 500-1240 MHz, the conductance tends to remain constant. In the remaining microwave range of frequency (1250-1800 MHz), the conductance sharply decreases with increasing signal frequency. In contrast to the behavior of the conductance which show increasing and decreasing trends of variations, the capacitance spectra shown in Fig. 5 (b) display only a decreasing trend of variation as signal frequency increases. The capacitance decreased from 120 pF to 2.9 pF as the frequency increases

from 10 MHz to 1800 MHz. While the behavior of the conductance suggests the presence of more than one current conduction mechanism in the devices [11, 19], the capacitance spectral response is ascribed to the dielectric response [11] to the incident signal frequency or to the continuous distribution of interface state [20]. Interfacial states are generated by defects. When the charges on the defects have no time to rearrange in response to the applied signal frequency, the capacitance starts decreasing with increasing signal frequency. When the current conduction mechanism is governed by the charge carrier quantum mechanical (QMT) tunneling and correlated barriers hopping (CBH), the total conductance show maximum peaks at the point where CBH becomes dominant over quantum mechanical tunneling [11, 19].

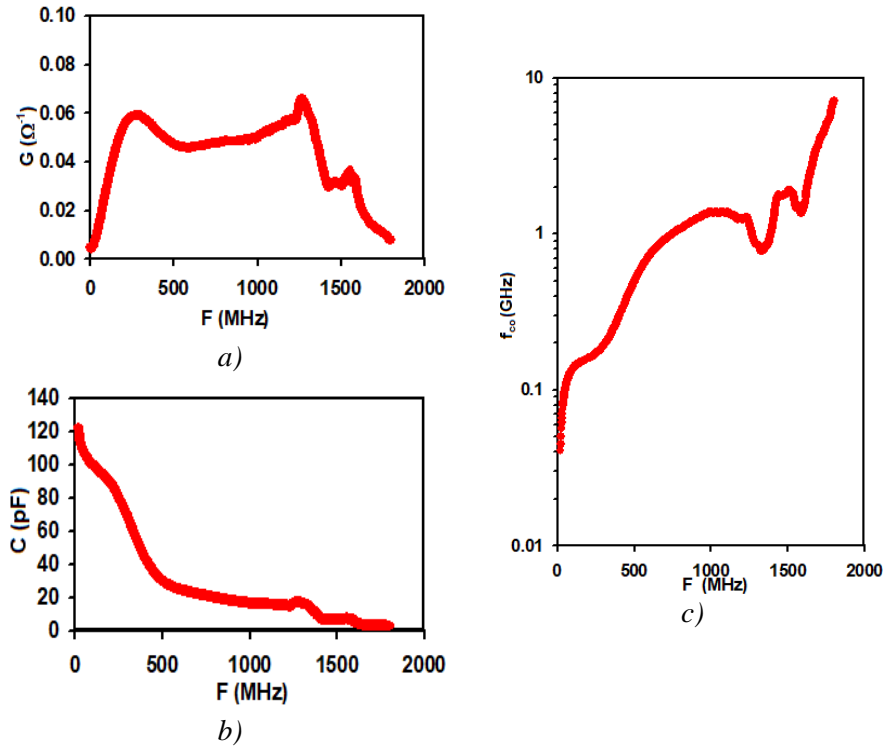


Fig. 5. (a) the conductance, (b) the capacitance and (c) the microwave cutoff frequency spectra for the Yb/InSe/Sb<sub>2</sub>Te<sub>3</sub>/Au heterojunction devices.

On the other hand, the microwave cutoff frequency spectra which are shown in Fig. 5 (c) indicated an increasing trend of variation with increasing signal frequency.  $f_{co}$  is the lowest frequency for which a mode will propagate in the device. For the device under study,  $f_{co}$  reaches 7.1 GHz at signal frequency of 1800 MHz. It is clear from the figure that wide range of selectivity of waves is possible. The transition of the microwave signals depends on the limiting frequency. This property makes the device usable as waveguides or band pass filters [19, 21].

It is also interesting to compare the currently designed device with other published devices. For the Yb/CdS/Sb<sub>2</sub>Te<sub>3</sub>/Ag devices [11], MOS device characteristics accompanied with resonance-antiresonance and negative capacitance effects were observed. This device was classified as tunneling devices in which the current and conductance transports are dominated by tunneling processes. For Yb/InSe/Sb<sub>2</sub>Te<sub>3</sub>/Au devices, no negative capacitance effects or resonance effects were observed. However wide frequency based tunability of the MOS device was identified. The current transport are dominated by the thermionic emission leading to very high current rectification ratios. Whilst Yb/CdS/Sb<sub>2</sub>Te<sub>3</sub>/Ag devices show a rectification ratio of 18.8, the current rectification ratio of the currently reported device reaches  $\sim 10^3$ . Other heterojunction devices which employ Sb<sub>2</sub>Te<sub>3</sub> as epilayer are also mentioned exhibiting smart applications [22]. Namely, Bi<sub>2</sub>Te<sub>3</sub>/Sb<sub>2</sub>Te<sub>3</sub> heterojunctions displayed thermophotovoltaic cell characteristics [22]. The

device successfully converted infrared light from dark and room-temperature surroundings into electricity.

#### 4. Conclusions

In the current study, we have shown that the construction of broken gap heterojunctions made of Yb/InSe/Sb<sub>2</sub>Te<sub>3</sub>/Au stacked layers could be beneficial for designing multifunctional devices. The electrical characterizations on the device proofed the usability of the device as frequency controllable MOS capacitors and as switching devices. The minimum “on/off” current ratios is  $\sim 10^3$ . It was also observed that the device could be employed as microwave cavities. Measurements of the conductance and capacitance spectra allowed identification of the microwave cutoff frequency of the cavities. Signal propagation cutoff limit is highly tunable and could reach 7.1 GHz. The features of the device nominate it for use in the active and passive modes of operations.

#### Acknowledgements

This project was funded by the Deanship of Scientific Research (DSR), University of Ha'il, Kingdom of Saudi Arabia under grant No. (BA-2005). The authors, therefore, gratefully acknowledge the DSR technical and financial support. This study was funded by the Deanship of Scientific Research (DSR), Ha'il University, Ha'il, Saudi Arabia under grant No. (BA-2005).

#### References

- [1] A. Ahmed, S. Han, *Scientific Reports* **10**(1), 1 (2020).
- [2] A. M. L. Marzo, R. Gusmão, Z. Sofer, M. Pumera, *Chemistry—A European Journal* **26**, 6583 (2020).
- [3] R-N. Verrone, Ch. Moisset, F. Lemarchand, A. Campos, M. Cabie, C. Perrin-Pellegrino, J. Lumeau, J.-Yves Natoli, K. Iliopoulos, *ACS Applied Nano Materials* **3**, 7963 (2020).
- [4] X. Zhang, Zh. Zhang, S. Song, Q. Zheng, W. Yu, W. Zheng, X. Zhu, H. Shao, J. Zhang, L. Chen, *Applied Physics Letters* **115**, 103105 (2019).
- [5] R. Mendoza-Pérez, J. Sastre-Hernández, M. A. Hernández-Pérez, J. Aguilar-Hernández, J. A. Del Oso, G. Santana-Rodríguez, J. J. Lizardi, *Materials Science in Semiconductor Processing* **112**, 104876 (2020).
- [6] S. R. Alharbi, A. F. Qasrawi, *Materials Science in Semiconductor Processing* **43**, 60 (2016).
- [7] Th. L. Anderson, H. B. Krause, *Acta Crystallographica Section B: Structural Crystallography and Crystal Chemistry* **30**, 1307 (1974).
- [8] N. M. Khusayfan, H. K. Khanfar, *Results in Physics* **10**, 332 (2018).
- [9] H. Águas, S. K. Ram, A. Araújo, D. Gaspar, A. Vicente, S. A. Filonovich, Elvira Fortunato, Rodrigo Martins, Isabel Ferreira, *Energy & Environmental Science* **4**, 4620 (2011).
- [10] H. Lind, S. Lidin, U. Häussermann, *Physical Review B* **72**, 184101 (2005).
- [11] N. M. Khusayfan, A. F. Qasrawi, H. K. Khanfar, *Materials Research Express* **5**, 026303 (2018).
- [12] S. M. Sze, K. K. Ng, *Physics of Semiconductor Devices*, John Wiley & sons, New Jersey, 2006.
- [13] A. Hospodková, E. Hulcius, J. Pangrác, F. Dominec, M. P. Mikhailova, A. I. Veinger, I. V. Kochman, *Journal of Crystal Growth* **464**, 206 (2017).
- [14] M. Mingebach, C. Deibel, V. Dyakonov, *Physical Review B* **84**, 153201 (2011).
- [15] N. M. Khusayfan, H. K. Khanfar, *Optik* **158**, 1154 (2018).
- [16] J. F. Prins, *Semiconductor science and technology* **18**, S125 (2003).
- [17] M. Gülnahar, *Superlattices and Microstructures* **76**, 394 (2014).
- [18] L. T. Horák, A. Vaško, M. Frumar, *Physica Status Solidi A* **14**, 289 (1972).

- [19] T. S. Kayed, A. F. Qasrawi, *Current Applied Physics* **20**, 114 (2020)
- [20] A. Dere, A. Tataroğlu, A. G. Al-Sehemi, A. A. Al-Ghamdi, F. F. El-Tantawy, W. A. Farooq, F. Yakuphanoglu, *Physica B: Condensed Matter* **520**, 76 (2017).
- [21] A. F. Qasrawi, H. D. Aloushi, *Materials Research Express* **6**, 086435 (2019).
- [22] X. Li, Ch. Lou, X. Li, Y. Zhang, B. Yin, Bi<sub>2</sub>Te<sub>3</sub>/Sb<sub>2</sub>Te<sub>3</sub> Heterojunction and Thermophotovoltaic Cells Absorbing the Radiation from Room-temperature Surroundings, arXiv preprint arXiv:1904.08808 (2019).